Measurement of directional atomic modulation direction using the azimuthal variation of first order Laue zone electron diffraction

Aurys Silinga[1], Christopher S. Allen[2,3], Juri Barthel[4], Colin Ophus[5], and Ian MacLaren[1],

1. *SUPA School of Physics and Astronomy, University of Glasgow, Glasgow G12 8QQ, UK*
2. *electron Physical Science Imaging Centre, Diamond Light Source Ltd., OX11 0DE, UK*
3. *Department of Materials, University of Oxford, Parks Road, Oxford OX1 3PH, UK*
4. *Ernst Ruska-Centre (ER-C 2), Forschungszentrum Jülich GmbH, 52425 Jülich, Germany*
5. *NCEM, Molecular Foundry, Lawrence Berkeley National Laboratory, Berkeley 94720, USA*

Abstract

We show that diffraction intensity into the First Order Laue Zone (FOLZ) of a crystal can have a strong azimuthal dependence, where this FOLZ ring appears solely because of unidirectional atom position modulation. Such a modulation was already known to cause the appearance of elliptical columns in atom resolution images, but we show that measurement of the angle via 4-dimensional Scanning Transmission Electron Microscopy (4DSTEM) is far more reliable and allows the measurement of the modulation direction with a precision of about 1° and an accuracy of about 3°. This method could be very powerful in characterising atomic structures in 3 dimensions by 4DSTEM, especially in cases where the structure deviates from that found in bulk crystals.

Atomic resolution imaging using scanning transmission electron microscopy (STEM) has been crucially important to our understanding of materials and artificial heterostructures for the past 30 years. This started with the widespread appreciation that High Angle Annular Dark Field (HAADF) imaging was mainly incoherent and strongly dependent on the atomic number *Z* of the species being imaged[1, 2], and only became more critical after the introduction of aberration-correction[3]. However, the majority of atomic-resolution imaging is purely concerned with a 2-dimensional projection of the sample, and not with the 3-dimensional structure, although inferences about modulation of atom positions along a column have been made from column shape analysis[4-6]. For this reason, analysis of column ellipticity has been included in open source analysis packages, such as *Atomap*, for quantification of atomic resolution images using Gaussian fitting[7].

Higher-order Laue zone (HOLZ) rings occur at relatively high diffracted angles and, due to the curvature of the Ewald sphere, have components of the diffraction vector along the beam direction. HOLZ rings therefore reveal information about the 3D atomic structure by revealing lattice spacings along the beam direction[8-10]. This has been used in STEM imaging with a modified conventional annular detector to show a period tripling in sodium cobaltate[11]. More recently, the advent of fast, pixelated direct electron detectors and the 4DSTEM technique[12, 13], has enabled high angle diffraction patterns to be acquired from every probe position on a scan. These patterns can then be analysed and quantified, leading to the development of high resolution HOLZ-STEM as a technique. This has been used to measure changes in crystal periodicity along the beam direction [14, 15], strain from the HOLZ ring radius[13], or atomic modulation at atomic resolution[16]. The present work exploits the azimuthal variation in the intensity of the First Order Laue Zone (FOLZ) rings, which can be measured in certain crystals due to atomic position modulation.

We performed STEM imaging along the $<110>_{cubic}$ direction of a sample of La_2CoMnO_6 (LCMO) grown on (111) LSAT, as previously characterised in Kleibeuker *et al.*[17], known to exhibit B-cation ordering, and expected to show atom modulation along La columns. Figure 1 is a schematic of the atomic structure, as refined by Bull *et al.*[18] and shows the unidirectional position modulation of the La atoms, which would be a zigzag if seen from the side. The modulation is of $\frac{1}{11.6}[010]$ in

crystal coordinates or 0.47Å along the $[010]$ direction. The component perpendicular to the [111] axis is about 0.2Å along the $[\bar{1}3\bar{1}]$ direction, which makes an angle of 35° to the normal to the $(\bar{1}10)$ plane (the vertical direction in Figure 1) (all standard crystallographic calculations from the structure of Bull *et al.*[18]).

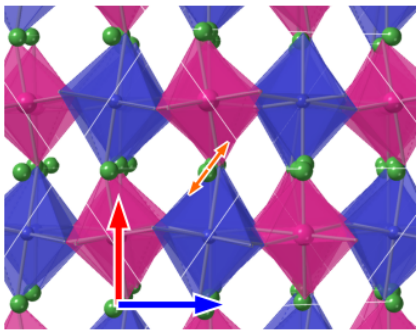

Figure 1: Schematic diagram of the atomic structure of La_2CoMnO_6 with the $[111]$ direction pointing upwards. La atoms are green, Co are blue and Mn magenta, O are at corners of octahedra and not shown, the modulation direction of the La atoms is indicated with an orange arrow. The normals to the $(\bar{1}10)$ and $(11\bar{2})$ planes are shown with red and blue arrows, respectively.

We recorded HAADF-STEM images, together with a 4DSTEM dataset at a camera length short enough to allow diffracted angles up to ~100 mrad to be recorded on the detector (as in MacLaren *et al.*[16]) from the same area. Nine such paired datasets were acquired with both good quality HAADF images and 4DSTEM datasets with diffraction patterns containing a HOLZ ring.

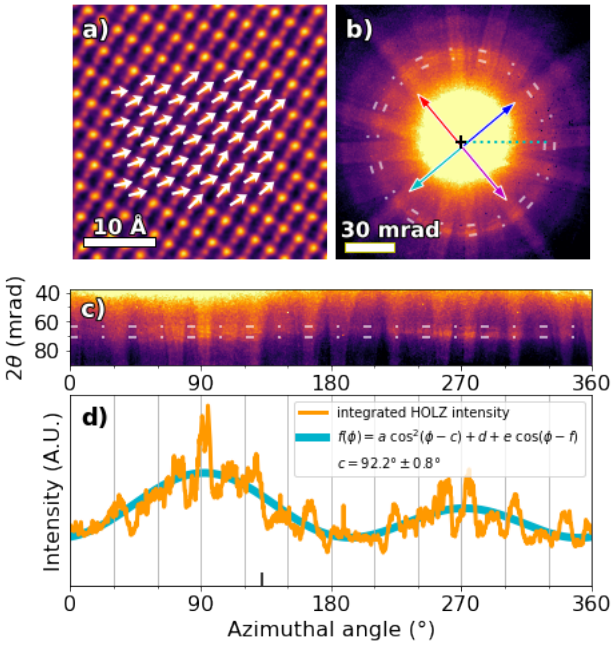

Figure 2. (a) HAADF atomic resolution image of modulated LCMO along a <110>cubic direction with ellipticity arrows superimposed for some columns, (b) Average STEM diffraction pattern for this region, (c) Polar transformation of the HOLZ ring (d) Azimuthal variation of average HOLZ ring intensity, the peak intensity occurs at c = 92.2 ± 0.8°. Figures 2b and 2c have had the contrast flattened by applying a power of 0.1 to the actual intensities to make visualisation of the real features at higher angles easier, but Figure 2d is calculated without any scaling of intensity.

We recorded the HAADF data as a sequence of 8 images, to enable post-processing correction of sample drift and scan distortions[19-21]. In this case, each was sequentially rotated by 90° and the image sequences were aligned and summed using the scanning drift correction code of Ophus *et al.*[21] to produce high signal-to-noise distortion-free images. We refined the atom positions using Atomap[7] and determined the ellipticity. An aligned HAADF-STEM sum image is shown in Figure 2a with arrows representing the evaluated ellipticity direction superimposed on La columns in the centre of the image. The average angle of ellipticity in this image was in the range of 20-38°, depending on the choice of fitting radius used for each atom column, which is discussed in more detail later.

For the same region, the diffraction pattern from a HOLZ-STEM dataset is shown in Figure 2b, with a clear FOLZ ring marked by the dotted lines. There is an obvious variation in intensity around the FOLZ ring, being highest at the top and bottom of the diffraction pattern whilst being almost invisible to the left and right. Figure 2c shows a polar transformation to a $2\theta - \phi$ description about the centre marked in 2b (performed with *emilys*, https://github.com/ju-bar/emilys), with a calibration of 2θ in mrad and ϕ in degrees. Again, dotted lines indicate the angular range in which most of the FOLZ intensity falls. We integrated the area inside the dotted lines to create the plot in Figure 2d. This was then fitted to the function:

$$I = a\cos^2(\phi - c) + d + e\cos(\phi - f) \qquad [1]$$

The first term captures the azimuthal intensity variation on the ring, the second the offset from zero intensity due to background high angle scattering, and the third any small tilt away from the zone axis leading to higher intensity in one azimuthal direction. Only the c term is significant to the present measurement as this gives the angle at which the FOLZ intensity peaks. This was measured as c = 92.2±0.8° for the dataset shown in Figure 2. To compare this to the ellipticity measurement from HAADF-STEM, the relative rotation of the diffraction pattern to the STEM scan direction needs to be known. For the optical setup used in this experiment the relative rotation angle was measured to be 110° (with positive angles in the counter-clockwise direction), making this angle 202.2°, or 22.2° (because of the 180° period of the function), consistent with the measured ellipticity from the HAADF image.

The four arrows from the centre in Figure 2b show the normals to the $(\bar{1}10)$ (red-magenta) and $(11\bar{2})$ (blue-cyan) planes (using the Kikuchi lines for orientation,

note plane normals are easier to measure directly in diffraction than crystal directions). There is a small deviation of the centre from the centre of the Laue zone due to slight sample mistilt from the $[111]$ zone axis. To get the rotation of the modulation from the $(\bar{1}10)$ plane normal, we subtracted the measured angle of the peak FOLZ intensity (92.2°) from the angle for the $(\bar{1}10)$ plane normal (the red arrow in the polar transform of Figure 2c) at 132°. This therefore measures the modulation direction as 37.2°±0.8° clockwise from the normal to $(\bar{1}10)$, in reasonable agreement with the structure refined by Bull *et al.*[18], where this angle was calculated as 35.1°.

Eight such measurements are shown in Figure 3 from different locations in the same sample (with some slight variations in thickness and crystal tilt across the specimen). We corrected the FOLZ data to crystal coordinates using the position of $(\bar{1}10)$ plane normal as seen in the polar transform. Error bars for each were calculated from the covariance of the *c* parameter in equation 1. The diffraction-based measurement is consistent in all cases with an average of 38.1±1.0°. We corrected the HAADF-STEM data to the same crystal coordinate system using the position of the $(\bar{1}10)$ plane normal, which was determined as part of *Atomap* fitting[7] to be at 56.9° (anticlockwise). All ellipticity measurements are smaller than this, meaning that all corrected measurements are clockwise rotations. These are plotted with an uncertainty estimated from the range of ellipse major axes given by *Atomap* fitting with different fit radii in the range of 25-45% of the nearest neighbour distance between atoms, combined with the random scatter in the measurement within each measured area (which was typically large). The average of all these measurements was a rotation of 40.2±10.2° clockwise. Clearly, this measurement is broadly consistent with the diffraction-based measurement and the crystallographic theory but there is much higher scatter in the measurement when using the ellipticity from HAADF images. This could be due to a number of factors. Details of the alignment procedure were tested by fitting with different codes, using different areas in the same image and this was found to be insignificant. The radius around the intensity maximum chosen for the ellipse fitting (as fractions of atom spacing) was found to be significant, and the apparent angle increased with increasing radius, probably because of the influence of tails of intensity from neighbouring B-site atom columns. It is possible also that residual microscope aberrations and sample mistilt have an effect and it is well known that even with zero drift of astigmatism and coma with time, the apparent aberrations can vary from one sample region to another. However, slow drift of coma and astigmatism with time are also often noted, and could be having an effect. We therefore conclude that measurements of ellipticity from an image based method are less accurate than the diffraction based methods (large scatter and possible systematic errors on image based measures of ellipticity was a problem previously noted when analysing data for Azough *et al.*[6] but not commented on in print at the time).

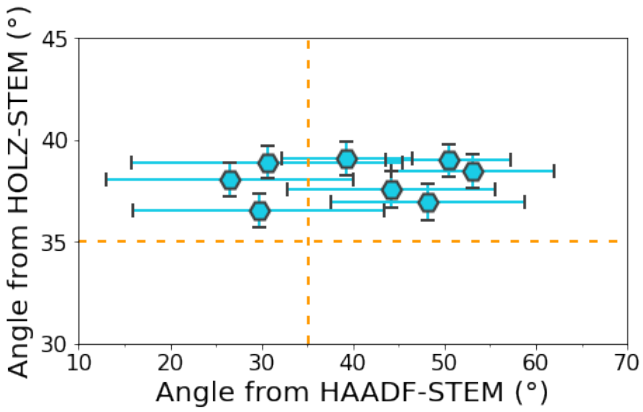

Figure 3. Correlation of atom modulation measurements from HOLZ-STEM and HAADF-. All angles are clockwise rotations from the $(\bar{1}10)$ plane normal. The expectations from the refinement of Bull et al.[18] are shown as orange dotted lines. Error bars are calculated from the standard deviation of each measurement, and including an uncertainty estimate from the variation as a result of fitting radius for the HAADF-STEM measurement.

The azimuthal variation on the FOLZ ring seen in the diffraction patterns (as exemplified by Figure 2b) agrees well with expectations from simulation. Figure 4a shows a simplistic kinematic calculation of diffracted intensities (which we calculated using *py4DSTEM*[22]) for a low convergence angle probe passing through the crystal in the same orientation as represented in Figure 1. There is a peak in FOLZ intensity along the in-plane component of the modulation direction, $[010]$, where the spacings of the planes responsible for reflections in the FOLZ would be most affected by La modulation along the beam direction (e.g. the $\bar{5}, 13, \bar{7}$ reflection in figure 4a). In contrast to this, there is very little intensity perpendicular to this (e.g. the very weak $12,1,\overline{12}$ spot indicated) where the plane spacing is almost unaffected by the La-modulation as the modulation is primarily within the diffracting planes, and structure factor will therefore remain very small. A more realistic simulation is shown in Figure 4b calculated by a multislice method using *Dr. Probe*[23] (full details in *Supplemental Materials*), showing the same azimuthal modulation, with the same peak and trough directions for intensity. Thus, whilst simple kinematic arguments using structure factors are quite illustrative,

the same trend holds in a fully dynamical calculation. Applying the same measurement as in Figure 2 on the simulated data in Figure 4b results in a calculated angle of 37.7±1.2°, in excellent agreement with the experimental measurement above of 38.1±0.8° (see *Supplemental Materials* for full details of this measurement).

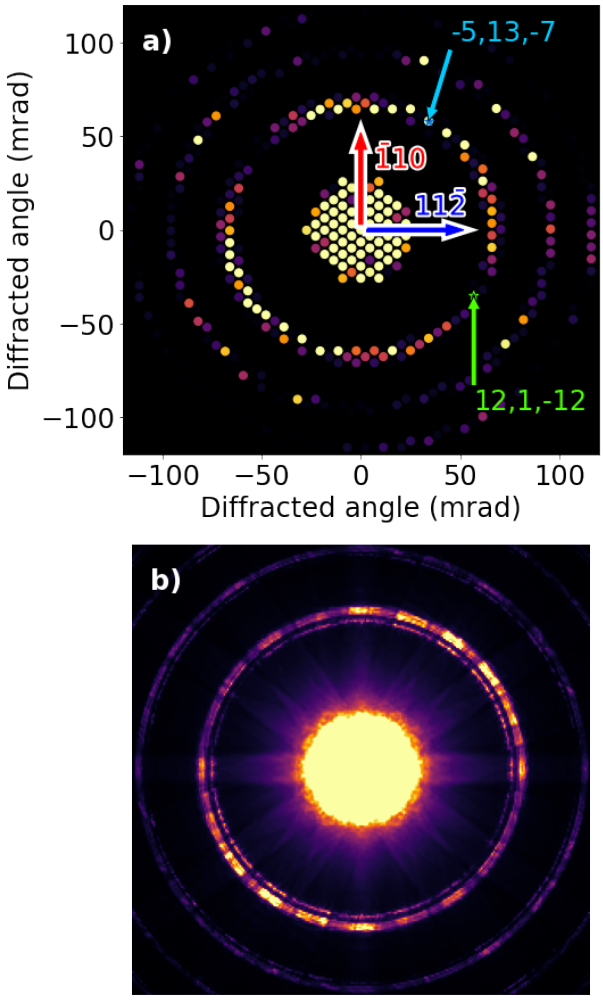

Figure 4:Simulated diffraction patterns of the structure shown in Figure 1 (with same crystal orientation): a) kinematic calculation of spot intensities with low convergence angle to allow individual diffraction spots to be distinguished, b) full multislice calculation for beam convergence angle close to that used in the experimental study.

It seems that there is a small discrepancy between a measurement of a 38.1° rotation of modulation direction from the $(\bar{1}10)$ plane normal and a crystallographic calculation of 35.1°. The fact that a similar discrepancy (of 37.7°) persists in simulations suggests that some feature of the measurement introduces a systematic error, for reasons that are not entirely clear. Possibly, the appearance of specific Kikuchi bands or reflections at specific angles introduces a slight bias away from the true direction (as the brightest parts on the FOLZ ring are at intersections with Kikuchi bands). As such, this method lacks the precision of refinement from neutron diffraction from bulk crystal[18]. Nevertheless, this has the major advantage of having a spatial resolution of nanometres or better. Moreover, a model-based approach of comparison of experiment with simulation can improve the quantitative interpretation. This would certainly be able to identify cases where the structure in a thin film deviates from the bulk structure, as previously noted for $LaFeO_3$[14], and thereby provide enough information to constrain a new DFT refinement. In the present case, it can be confirmed with the aid of the simulation that the thin film structure shows no detectable deviation from the bulk structure for La_2CoMnO_6 previously refined by Bull *et al.*[18].

In conclusion, we show that the first order Laue zone of an ordered structure can have a strong, approximately sinusoidal azimuthal intensity dependence, and that this correlates with and therefore reveals the direction of the atom modulation that gave rise to it. Measurement of modulation direction via the azimuthal intensity variation in diffraction is both easier and more reliable than column shape analysis from atomic resolution imaging. Such azimuthal variation is also visible in other materials, such as Figure 3 in our previous work[16]. Whilst this azimuthal variation still lacks some of the three-dimensional information available in a good neutron diffraction refinement[18], this technique opens up new possibilities for three dimensional studies of crystallography on the nanoscale, which therefore serves as a valuable complement to neutron or X-ray diffraction. These new possibilities could include spatial variations in atomic modulation direction and strength in response to strain or chemistry, such as within epitaxial heterostructures and core-shell structures.

Acknowledgements

We thank Diamond Light Source for access and support in use of the electron Physical Science Imaging Centre (Instrument E02, proposal number MG27893) that contributed to the results presented here . Work at the Molecular Foundry was supported by the Office of Science, Office of Basic Energy Sciences, of the U.S. Department of Energy under Contract No. DE-AC02-05CH11231. The authors gratefully acknowledge Steven Zeltmann at the Lawrence Berkeley National Laboratory for assistance with *py4DSTEM.* The sample was provided by Dr J.E. Kleibeuker and Prof. J.L. Driscoll of the University of Cambridge. The first version of the code for calculating Figure 4a was initially developed in

an undergraduate research project with the aid of Mr Joss Thompson.

References

1. S. J. Pennycook and D. E. Jesson, Ultramicroscopy **37** (1-4), 14-38 (1991).
2. P. Hartel, H. Rose and C. Dinges, Ultramicroscopy **63** (2), 93-114 (1996).
3. I. MacLaren and Q. M. Ramasse, Int. Mater. Rev. **59** (3), 115-131 (2014).
4. A. Borisevich, O. S. Ovchinnikov, H. J. Chang, M. P. Oxley, P. Yu, J. Seidel, E. A. Eliseev, A. N. Morozovska, R. Ramesh, S. J. Pennycook and S. V. Kalinin, ACS Nano **4** (10), 6071-6079 (2010).
5. Q. He, R. Ishikawa, A. R. Lupini, L. Qiao, E. J. Moon, O. Ovchinnikov, S. J. May, M. D. Biegalski and A. Y. Borisevich, ACS Nano **9** (8), 8412-8419 (2015).
6. F. Azough, R. I. Cernik, B. Schaffer, D. Kepaptsoglou, Q. M. Ramasse, M. Bigatti, A. Ali, I. MacLaren, J. Barthel, M. Molinari, J. D. Baran, S. C. Parker and R. Freer, Inorg Chem **55** (7), 3338-3350 (2016).
7. M. Nord, P. E. Vullum, I. MacLaren, T. Tybell and R. Holmestad, Advanced Structural and Chemical Imaging **3** (2017).
8. P. M. Jones, G. M. Rackham and J. W. Steeds, Proc. R. Soc. London Ser. A-Math. Phys. Eng. Sci. **354**, 197-222 (1977).
9. D. E. Jesson and J. W. Steeds, Philosophical Magazine A **61** (3), 363-384 (1990).
10. J. C. H. Spence and C. Koch, Philosophical Magazine B-Physics of Condensed Matter Statistical Mechanics Electronic Optical and Magnetic Properties **81** (11), 1701-1711 (2001).
11. F. T. Huang, A. Gloter, M. W. Chu, F. C. Chou, G. J. Shu, L. K. Liu, C. H. Chen and C. Colliex, Phys. Rev. Lett. **105** (12) (2010).
12. C. Ophus, Microsc. Microanal. **25** (3), 563-582 (2019).
13. I. MacLaren, T. A. Macgregor, C. S. Allen and A. I. Kirkland, APL Materials **8** (11), 110901 (2020).
14. M. Nord, A. Ross, D. McGrouther, J. Barthel, M. Moreau, I. Hallsteinsen, T. Tybell and I. MacLaren, Physical Review Materials **3** (6), 063605 (2019).
15. G. W. Paterson, R. W. H. Webster, A. Ross, K. A. Paton, T. A. Macgregor, D. McGrouther, I. MacLaren and M. Nord, Microsc. Microanal. **26** (5), 944-963 (2020).
16. M. Nord, J. Barthel, C. S. Allen, D. McGrouther, A. I. Kirkland and I. MacLaren, Ultramicroscopy **226**, 113296 (2021).
17. J. E. Kleibeuker, E.-M. Choi, E. D. Jones, T.-M. Yu, B. Sala, B. A. MacLaren, D. Kepaptsoglou, D. Hernandez-Maldonado, Q. M. Ramasse, L. Jones, J. Barthel, I. MacLaren and J. L. MacManus-Driscoll, NPG Asia Materials **9** (2017).
18. C. L. Bull, H. Y. Playford, K. S. Knight, G. B. G. Stenning and M. G. Tucker, Phys. Rev. B **94** (1), 014102 (2016).
19. X. Sang and J. M. LeBeau, Ultramicroscopy **138**, 28-35 (2014).
20. L. Jones, H. Yang, T. J. Pennycook, M. S. J. Marshall, S. Van Aert, N. D. Browning, M. R. Castell and P. D. Nellist, Advanced Structural and Chemical Imaging **1** (2015).
21. C. Ophus, J. Ciston and C. T. Nelson, Ultramicroscopy **162**, 1-9 (2016).
22. B. H. Savitzky, S. E. Zeltmann, L. A. Hughes, H. G. Brown, S. Zhao, P. M. Pelz, T. C. Pekin, E. S. Barnard, J. Donohue, L. Rangel DaCosta, E. Kennedy, Y. Xie, M. T. Janish, M. M. Schneider, P. Herring, C. Gopal, A. Anapolsky, R. Dhall, K. C. Bustillo, P. Ercius, M. C. Scott, J. Ciston, A. M. Minor and C. Ophus, Microsc. Microanal. **27** (4), 712-743 (2021).
23. J. Barthel, Ultramicroscopy **193**, 1-11 (2018).

Measurement of directional atomic modulation direction using the azimuthal variation of first order Laue zone electron diffraction

Aurys Silinga[1], Christopher S. Allen[2,3], Juri Barthel[4], Colin Ophus[5], Ian MacLaren[1],

1. *SUPA School of Physics and Astronomy, University of Glasgow, Glasgow G12 8QQ, UK*
2. *electron Physical Science Imaging Centre, Diamond Light Source Ltd., OX11 0DE, UK*
3. *Department of Materials, University of Oxford, Parks Road, Oxford OX1 3PH, UK*
4. *Ernst Ruska-Centre (ER-C 2), Forschungszentrum Jülich GmbH, 52425 Jülich, Germany*
5. *NCEM, Molecular Foundry, Lawrence Berkeley National Laboratory, Berkeley 94720, USA*

Supplemental Materials

Microscopy and data-processing methods

The LCMO sample was imaged using the E02 instrument in the EPSIC facility at Diamond light source. This is a JEOL ARM300F, and was operated at 200 kV, with a probe convergence angle of ~20 mrad, both to record HAADF images and to record 4DSTEM datasets to the Merlin EM detector (a 2x2 tiled detector mounted below the viewing screen).

HAADF images were recorded as 8 sequential images and then aligned and summed using the software of Ophus *et al*.[1]. As stated in the manuscript, atom positions were found and fitted, and the ellipticity determined using https://atomap.org/. Normal mean and standard deviation for the ellipticity direction was determined using standard *numpy* functions.

4DSTEM datasets containing large angular range diffraction patterns were processed by the following procedure:

- Datasets were loaded with hyperspy (https://hyperspy.org/) and filtered to remove dead and hot pixels (https://pixstem.org/using_pixelated_stem_class.html#finding-and-removing-bad-pixels), and then resaved
- Nine image areas were defined in each dataset for analysis in a 3x3 grid and the sum diffraction pattern calculated for each of the nine.

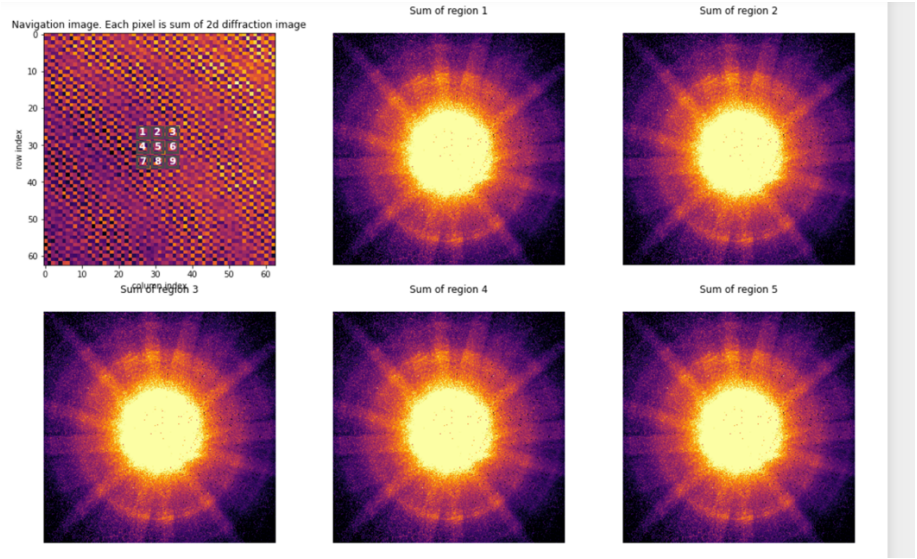

Figure S1: calculating average diffraction patterns from small areas in the 4DSTEM dataset

- The polar transform about the pattern centre (found by trial and error) was calculated using the *Emilys* package (https://github.com/ju-bar/emilys). At the radius of the ring, (about 180 pixels), it was chosen to sample the azimuthal direction in $\approx 2\pi r$ samples to keep a similar

azimuthal sampling to the pixel size, which meant us choosing to use a sampling of 1080 pixels (i.e. 1/3° divisions).

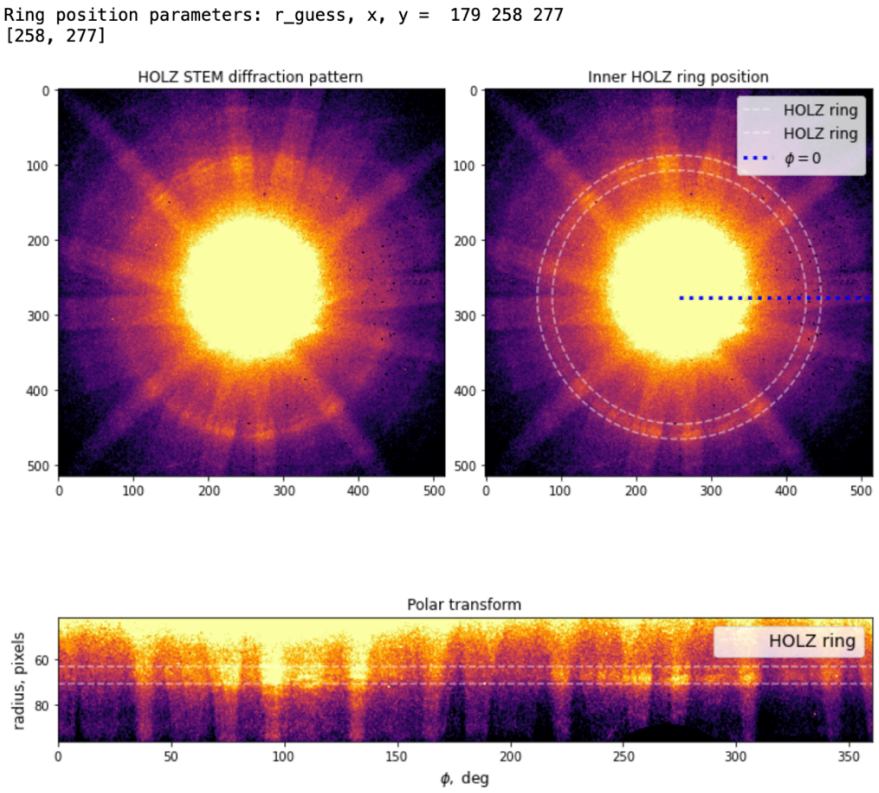

Figure S2 polar transform of one diffraction pattern, after finding the centre of the FOLZ.

- The resulting polar transformed diffraction patterns were summed into 1D line profiles in a width of ±10 pixels about the ideal radius
- This was fitted using *scipy.optimize* to the function described, and the angle shift parameter for the $\cos^2$ function was extracted.

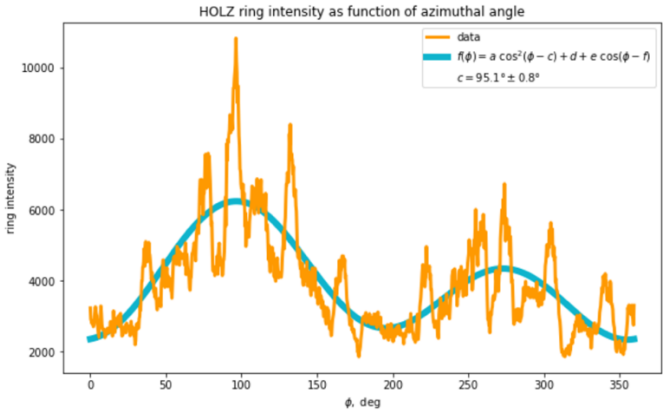


```
a,c,d,e,f = [2701.2518541077807, 95.05369498155156, 2585.2987953444012, 963.3197574850659, 104.89092912797996] +/-
[77.56385591226567, 0.8225966775575233, 47.49796735935611, 38.781927883380526, 2.306649249974957]
region 2
```

Fig S3: 1D sum of the FOLZ, fit plot, and fit parameters.

- Diffraction to image rotation was determined by scanning a defocused probe with a recognisable feature in a shadow image, and then rotating the diffraction pattern in the dataset until moving along the two orthogonal scan axes moves the shadow image in the correct directions.

Full results

A full table of results is presented below in Table S1 for the different datasets used, which contained a pair of a good HAADF image and a good 4DSTEM dataset.

	Fitting radius (as a fraction of nearest neighbour distance)					
Timestamp	**0.25**	**0.30**	**0.35**	**0.40**	**0.45**	**FOLZ**
154716	48.7 ± 11.0 (1.22)	47.7 ± 9.9 (1.21)	45.5 ± 9.9 (1.19)	42.1 ± 10.0 (1.17)	37.0 ± 10.7 (1.16)	37.6 ± 0.9
160139	34.7 ± 15.5 (1.16)	32.7 ± 13.7 (1.15)	30.4 ± 12.8 (1.15)	27.2 ± 11.8 (1.15)	23.3 ± 10.8 (1.15)	36.5 ± 0.8
160712	39.5 ± 16.6 (1.19)	35.3 ± 14.2 (1.18)	31.2 ± 12.9 (1.18)	25.9 ± 11.2 (1.19)	21.0 ± 9.8 (1.2)	38.9 ± 0.8
161216	31.2 ± 17.3 (1.18)	28.8 ± 14.0 (1.19)	26.9 ± 12.1 (1.2)	24.3 ± 10.9 (1.21)	21.5 ± 10.2 (1.23)	38.0 ± 0.8
162329	41.0 ± 8.1 (1.31)	40.8 ± 6.8 (1.31)	40.2 ± 6.3 (1.31)	38.6 ± 6.2 (1.29)	36.1 ± 6.5 (1.28)	39.1 ± 0.8
162847	50.5 ± 7.2 (1.33)	50.8 ± 6.5 (1.33)	50.8 ± 6.4 (1.31)	50.4 ± 6.6 (1.29)	49.6 ± 7.1 (1.27)	39.0 ± 0.8
163337	56.2 ± 10.7 (1.25)	55.0 ± 8.2 (1.24)	53.4 ± 7.7 (1.23)	51.6 ± 7.5 (1.22)	49.0 ± 8.2 (1.2)	38.4 ± 0.8
163801	51.8 ± 9.4 (1.26)	50.6 ± 9.5 (1.24)	48.9 ± 9.6 (1.21)	46.3 ± 10.3 (1.19)	42.9 ± 11.1 (1.17)	37.0 ± 0.9

Table S1: Ellipticity data from Atomap with FOLZ azimuthal peak position data. Ellipticity angles with standard deviations for each dataset (by timestamp) are given for five different ditting radii. The actual ellipticity (ratio of major and minor axes) is in brackets in each case. The relatively small ellipticity values may be contributing to the high random uncertainties.

Simulation of diffraction patterns

The simple disc diffraction pattern of Figure 4a was calculated using intensities from a simple kinematic calculation in *py4dstem*[2] plotted using custom plotting code using *matplotlib*.

The dynamical calculation of Figure 4b was calculated using Dr Probe[3] using the following parameters:

- Acceleration voltage 200 kV
- Beam direction [111]
- Convergence semiangle 20 mrad
- Sample thickness 50 nm
- Angular range simulated 120 mrad
- Sampling in diffraction plane 384×384 pixels
- Pixel size 0.8068 mrad/pixel
- Calculation precision float-32
- Structure Bull *et al*.[4]

Polar transform and fitting of the simulated pattern

Polar transform was performed on .

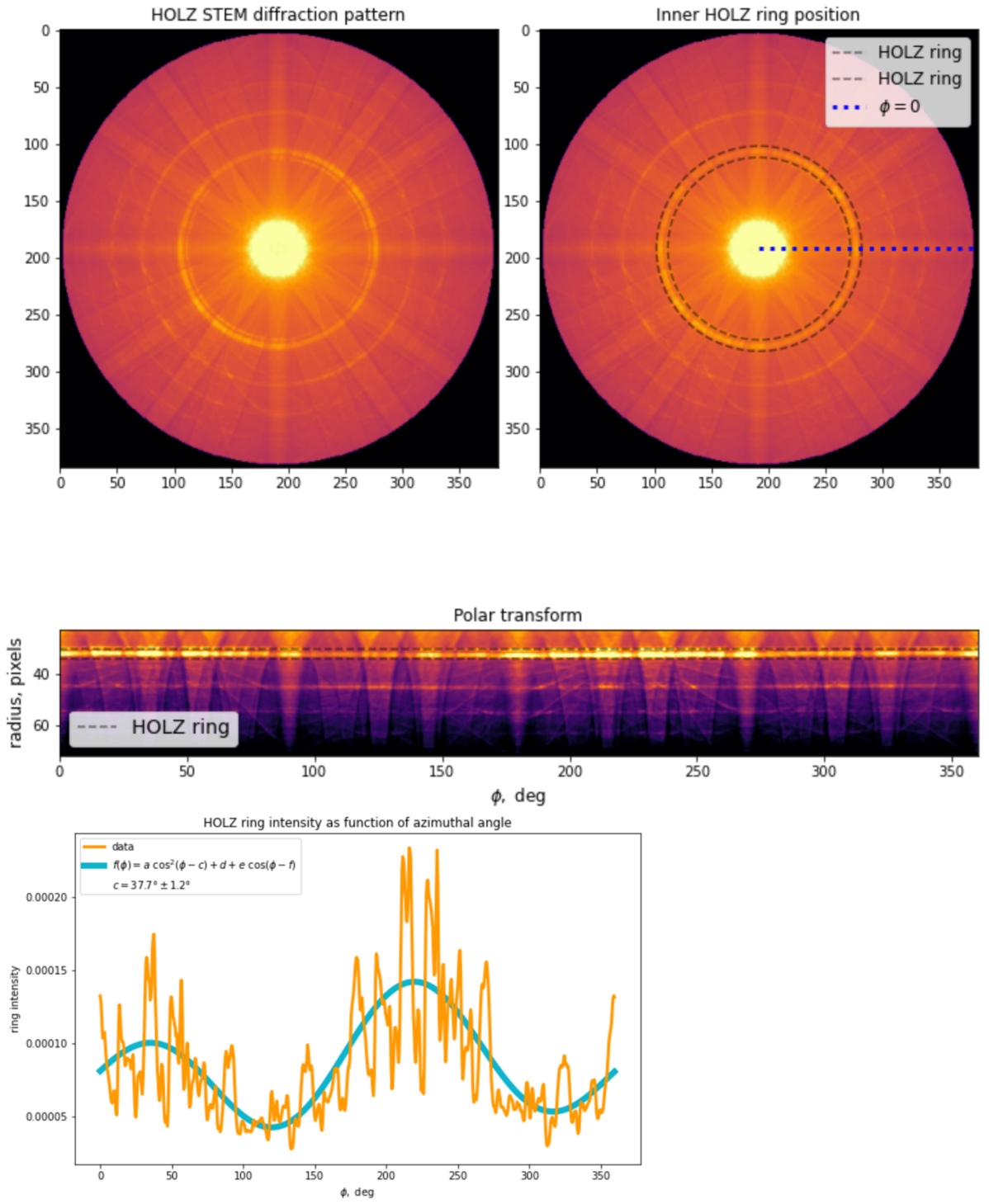

a,c,d,e,f = [7.157274082514289e-05, 37.74813102524245, 4.934995974633684e-05, 2.1565477985098358e-05, 232.396734999
23148] +/- [2.923141209505613e-06, 1.1700240366623762, 1.790051102347615e-06, 1.461570604752765e-06, 3.883142639135
6123]

Fig S4: Polar transform of the simulated diffraction pattern and the fitting of the azimuthal intensity modulation therein to give a peak intensity at 37.7°.

Open data deposit

The main Jupyter notebooks used for processing the data and some example datasets will be deposited in a repository (to be advertised) for further inspection or use by interested readers.

References

1. C. Ophus, J. Ciston and C. T. Nelson, Ultramicroscopy **162**, 1-9 (2016).
2. B. H. Savitzky, S. E. Zeltmann, L. A. Hughes, H. G. Brown, S. Zhao, P. M. Pelz, T. C. Pekin, E. S. Barnard, J. Donohue, L. Rangel DaCosta, E. Kennedy, Y. Xie, M. T. Janish, M. M. Schneider, P. Herring, C. Gopal, A. Anapolsky, R. Dhall, K. C. Bustillo, P. Ercius, M. C. Scott, J. Ciston, A. M. Minor and C. Ophus, Microsc. Microanal. **27** (4), 712-743 (2021).
3. J. Barthel, Ultramicroscopy **193**, 1-11 (2018).
4. C. L. Bull, H. Y. Playford, K. S. Knight, G. B. G. Stenning and M. G. Tucker, Phys. Rev. B **94** (1), 014102 (2016).